

Echoes from the scattering of wavepackets on wormholes

José T. Gálvez Ghersi,^{1,*} Andrei V. Frolov,^{1,†} and David Dobre^{1,‡}

¹*Department of Physics, Simon Fraser University, Burnaby, BC, V5A 1S6, Canada*

In the light of the recent progress showing that the hypothetical observation of pulses isolated from the gravitational radiation transient (also known as echoes) would prove the existence of exotic compact objects (ECOs); it is possible to reproduce many features of the ringdown signal by simulating a scattering problem instead of the full coalescence of ECOs. In this paper, we study the dynamics of scalar and tensor wavepackets colliding against a spherically symmetric traversable wormhole. Our purpose is to extract the features of the time-dependent scattering solutions inside and outside the effective potential cavity in addition to their asymptotic behavior. Using the geometrical optics approximation, we show that the amplitude of the echoes is only large enough in a narrow bandwidth of frequency space, where the intensity of the transient reduces. The computer code used to produce these results is publicly available for further applications, including scattering and accretion processes.

I. INTRODUCTION

The era of gravitational wave (GW) astronomy [1, 2] has begun. GW spectroscopy, in contrast to its atomic counterpart, allows us to characterize strong gravitational interactions in their radiative regime. In this new range of frequencies, it is now possible to explore the role of dynamical gravitational degrees of freedom in a wide range of astrophysical [3, 4] and cosmological [5, 6] phenomena.

The prolonged absence of observational evidence confirming the dynamical properties of spacetime has motivated a plethora of conjectures about the behaviour of gravity within and beyond [7–9] classical General Relativity (GR). Latterly, the potential existence of exotic compact objects (ECOs) sourced by quantum effects on gravity [10–12] (such as wormholes, firewalls and gravastars) has captured the attention of many recent efforts [13–15]. Wherein the primary claim is that the detection of a train of “echoes” isolated from the main transient of GW and with generically large amplitudes would be clear evidence of ECOs. It is, therefore, necessary to understand (i) the mechanisms behind the production of echoes and (ii) the intensity and spectrum of the outgoing wavelets compared to the GW transient in the most straightforward possible setup. In this paper, we explore the generation of echoes by colliding wavepackets of scalar and tensor radiation against a traversable spherically symmetric wormhole [16]. Such a wormhole behaves just like a Fabry-Perot cavity, shares common properties with the effective potential cavities made by other ECOs, like gravastars and firewalls, and the main features of the dispersed pulses are similar to the ringdown signals after the coalescence of ECOs.

Here we consider a wormhole configuration made by the junction of two Schwarzschild geometries of equal

masses at $r_0 > 2M$, just as shown in [13]. In this case, the symmetry of the centrifugal barriers at $r = 3M$ on each side of the throat allows us to find the reflection and transmission coefficients of the cavity. Hence, it is possible to reconstruct the spectral shape of the outgoing pulse using the geometrical optics approximation. Nevertheless, this approximation predicts an exponential decay of the subsequent higher order reflections, which appears instead as a power law in the full solution of the scattering problem. Thus, the excitation of quasinormal modes (QNM) is the only cause for the presence of echoes in the time evolving profile, these modes are sourced by a sequence of internal reflections inside the potential cavity and then propagate throughout the surface of the maximal potential energy spheres (i.e., the “edges” of the potential barriers), while leaking energy into the exterior. QNMs of the Schwarzschild solution have been extensively studied and reproduced in various analytic and numerical simulations [17, 18]; thus it is easy to identify their characteristic frequencies in the spectrum of outgoing pulses. We as well present the full scattering solution both inside and outside the wormhole cavity in detail, along with the energy fluxes and the asymptotic solutions for the principal spherical modes of a scalar (and tensor) wavepackets. In addition to this, we find the width and frequency intervals contained in the incident wavepackets for which the outgoing wavelets have maximal amplitudes. Our computer code is optimized to solve both scalar accretion and scattering problems and is publicly available in <https://github.com/andrei-v-frolov/accretion/tree/wormhole>.

The layout for this paper is as follows: in section II, we review the scattering problem of scalar waves starting by a quick overview of the dispersion of a Gaussian pulse by a Schwarzschild black hole. In this review, we will be able to calculate the transmission and reflection coefficients of the centrifugal barriers constituting the walls of the resonant cavity in the case of the wormhole. Our results show a frequency “sweet spot” such that the incident pulse is not fully reflected nor fully transmitted by the cavity, favouring multiple internal reflections that source the QNMs. Furthermore, we solve the scattering problem

* joseg@sfu.ca

† frolov@sfu.ca

‡ ddobre@sfu.ca

by a wormhole directly using the same ingoing Gaussian wavepacket, and then we compare the Fourier transform of this solution with the pulse reconstructed following the geometrical optics approximation. We find that the approximate reconstruction matches the full solution, up to the peaks due to the QNM frequencies. Likewise, we evaluate the amplitude of each of the echoes as a function of the width of the initial gaussian waveform, finding that a single width of the incident pulse maximizes the amplitude of each echo. In section III, we extend all the results in the previous section for a Gaussian pulse of tensor fluctuations of the metric by following the even and odd decomposition of the tensor modes introduced by Regge, Wheeler and Zerilli in [19–22]. Our results can be recasted in terms of the usual asymptotic polarization modes h_+ and h_\times , known as the perturbations of a flat metric. Finally, in section IV, we discuss and conclude.

II. SCATTERING OF SCALAR WAVEPACKETS

In this section, we solve the scattering of a Gaussian wavepacket by a spherically symmetric wormhole. To do so, we will first review the dispersion by the centrifugal barrier of a spherically symmetric black hole in order to find the properties of the potential cavity.

A. Scattering by a Schwarzschild black hole

The dispersion of scalar waves by a Schwarzschild black hole has been thoroughly studied [23–26], it is crucial for our purposes to provide the full solution since it contains all the information of the potential barriers constituting the effective potential in the case of a wormhole. The dynamics of the scattering problem is found by solving the equation of motion for scalar field

$$\square\Phi = 0, \quad (1)$$

where $\square \equiv g^{\alpha\beta}\nabla_\alpha\nabla_\beta$ is the standard d'Alembertian in a curved background. Here $g_{\alpha\beta}$ is the metric tensor in a spherically symmetric Schwarzschild-like static spacetime

$$g_{\alpha\beta} = -f(r)\delta_\alpha^t\delta_\beta^t + \frac{1}{f(r)}\delta_\alpha^r\delta_\beta^r + r^2\left(\delta_\alpha^\theta\delta_\beta^\theta + \sin^2\theta\delta_\alpha^\phi\delta_\beta^\phi\right). \quad (2)$$

It is convenient to introduce the tortoise coordinate x :

$$x \equiv \int_{r_0}^r \frac{dr}{f(r)}, \quad (3)$$

In the case of the Schwarzschild metric $f(r) = 1 - r_g/r$ the last expression yields

$$x = r - r_0 + r_g \ln\left(\frac{r - r_g}{r_0 - r_g}\right), \quad (4)$$

for $r_g < r < +\infty$ and $r_0 > r_g$, where $r_g = 2M$ is the usual Schwarzschild radius. By direct evaluation, we see

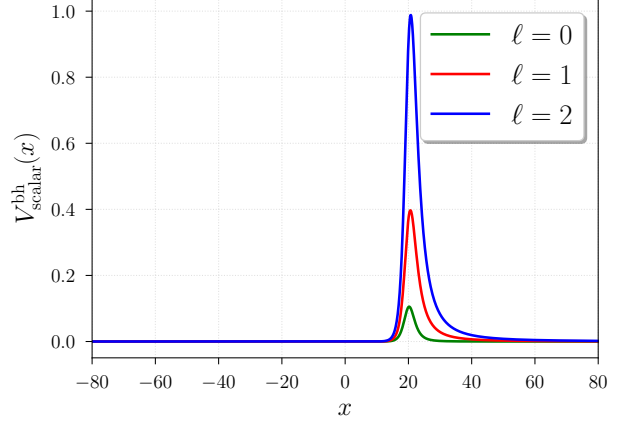


FIG. 1. Effective potential for the spherical modes $\mathcal{U}_{20}^{\text{bh}}(x, t)$ scattered by a Schwarzschild black hole, growing with ℓ . The wall acts as a barrier transparent to certain frequencies above a transmissivity threshold and reflective for lower frequencies.

that $r = r_0$ corresponds to $x = 0$, the horizon $r = 2M$ maps into $x \rightarrow -\infty$ and $r \rightarrow +\infty$ is $x \rightarrow +\infty$. In our numerical routine, we invert (4) to get $r \equiv r(x)$ (see the appendix A, subsection 6 in [3] for more details). In tortoise coordinates, we can decompose the scalar field in spherical harmonics

$$\Phi(x, t) = \frac{1}{r(x)} \sum_{\ell, m=0} \mathcal{U}_{\ell m}^{\text{bh}}(x, t) Y_{\ell m}(\theta, \phi), \quad (5)$$

in that way we can rewrite (1) as

$$[-\partial_t^2 + \partial_x^2 - V_{\text{scalar}}(x)] \mathcal{U}_{\ell m}^{\text{bh}}(x, t) = 0, \quad (6)$$

and the effective potential $V_{\text{scalar}}(x)$ is given by

$$V_{\text{scalar}}(x) = \left(1 - \frac{r_g}{r(x)}\right) \left[\frac{\ell(\ell+1)}{r(x)^2} + \frac{r_g}{r(x)^3} \right]. \quad (7)$$

After rearranging the variables, the equation of motion of the spherical modes is now written in its traditional linear waveform. In Fig. 1, we observe the growth of the potential barrier with the quantum number ℓ . The potential wall does not vanish for the monopole ($\ell = 0$) due to the extra term proportional to r^{-3} appearing after the coordinate change, which replaces the radial damping in the original Schwarzschild coordinates (t, r) . Such a term becomes subdominant for all $\ell \geq 1$. Intuitively, it is reasonable to expect that the modes with frequency above a given threshold can cross the barrier, while reflecting the lower frequency modes.

Now we setup the scattering problem for one of the spherical modes ($\mathcal{U}_{20}^{\text{bh}}$, the quadrupole) with the following initial conditions corresponding to an ingoing Gaussian wavepacket

$$\mathcal{U}_{20}^{\text{bh}}(x, 0) = \exp\left(\frac{(x - x_0)^2}{2\sigma^2}\right), \quad \left.\frac{d\mathcal{U}_{20}^{\text{bh}}}{dt}\right|_{t=0} = \frac{d\mathcal{U}_{20}^{\text{bh}}(x, 0)}{dx}, \quad (8)$$

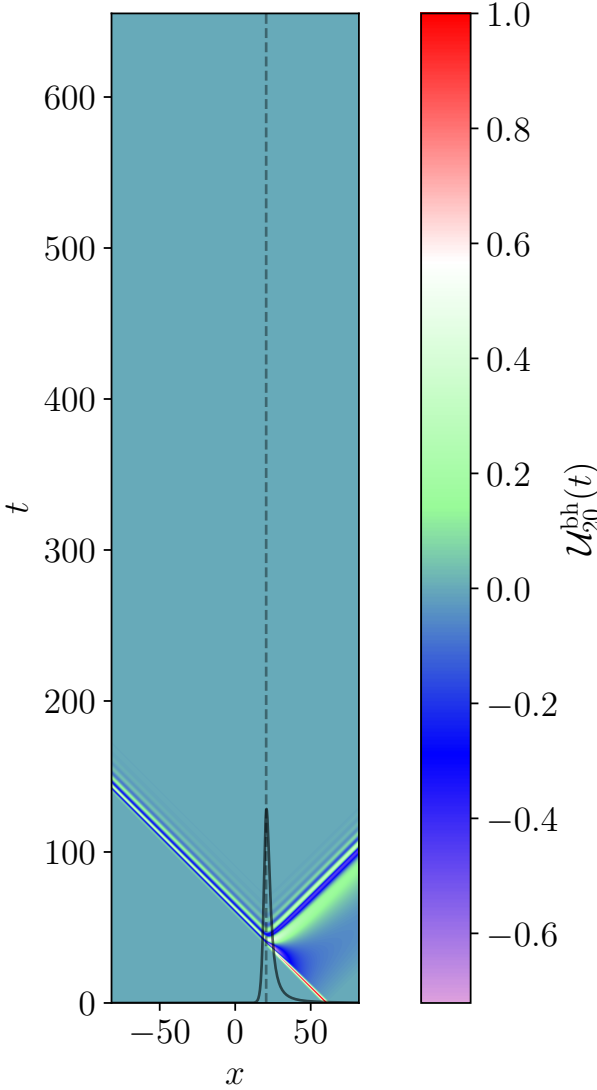


FIG. 2. Dispersion of the ingoing Gaussian wavepacket $\mathcal{U}_{20}^{\text{bh}}$ by the potential barrier (plotted in black) showing the incident, reflected and transmitted pulses, it is possible notice the ringing of the reflected solution due to the quasinormal modes.

After fixing the values of the width to be $\sigma = 0.9185r_g$, the initial position of the Gaussian at $x_0 = 60.0r_g$, $r_0 = 20.0r_g$ and the initial conditions in (8), we show the time-dependent solution of (6) in Fig. 2, where we distinguish the incident, transmitted and reflected parts of the solution. It is important to observe the absence of spurious late time reflections and interferences due to the implementation of perfectly matching layers (PMLs) in the outermost regions of our simulation box (see the details of our setup for PMLs in [3]). We observe the main features of the reflected signal in Fig. 3, where the asymptotic behavior of the signal shows a sharp transient is a consequence of the collision against the potential wall, and the ringing of quasinormal modes occurring right after the reflection in agreement with [27].

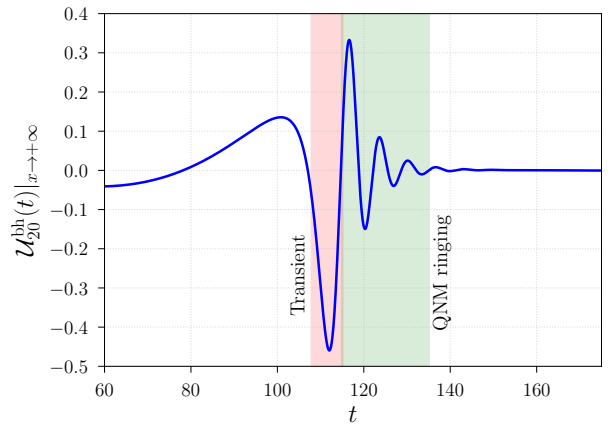


FIG. 3. Asymptotic solution for the quadrupole mode $\mathcal{U}_{20}^{\text{bh}}(x, t)$ by direct evaluation of the results in Fig. 2. The reflected signal shows its maximum peak and the posterior ringing due to QNMs.

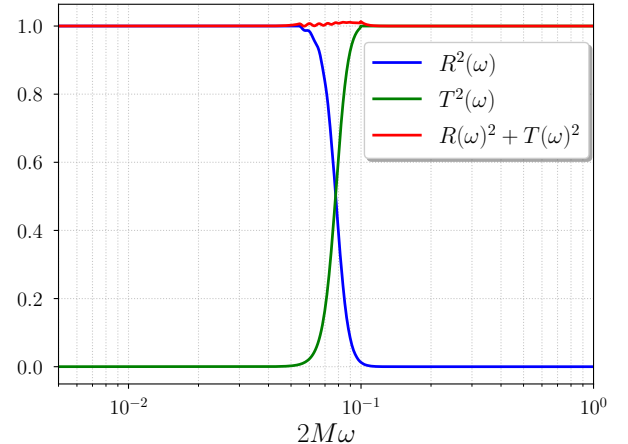


FIG. 4. Reflection and transmission coefficients as a function of frequency (ω), the identity $R^2 + T^2 = 1$ is fulfilled with an error smaller than 1%.

It is now possible to evaluate the reflection and transmission coefficients of the potential wall depicted in Fig. 1. To do so, we compute the one dimensional Fourier transform of the incident $\tilde{\mathcal{U}}_{20}^{\text{inc}}(\omega) = \mathcal{F}[\mathcal{U}_{20}^{\text{bh}}(0, x)]$, reflected $\tilde{\mathcal{U}}_{20}^{\text{ref}}(\omega) = \mathcal{F}[\mathcal{U}_{20}^{\text{bh}}(t, +\infty)]$ and transmitted $\tilde{\mathcal{U}}_{20}^{\text{trans}}(\omega) = \mathcal{F}[\mathcal{U}_{20}^{\text{bh}}(t, -\infty)]$ from the solved scattering modes in order to define

$$R(\omega) \equiv \frac{\|\tilde{\mathcal{U}}_{20}^{\text{ref}}(\omega)\|}{\|\tilde{\mathcal{U}}_{20}^{\text{inc}}(\omega)\|}, \quad T(\omega) \equiv \frac{\|\tilde{\mathcal{U}}_{20}^{\text{trans}}(\omega)\|}{\|\tilde{\mathcal{U}}_{20}^{\text{inc}}(\omega)\|} \quad (9)$$

as the transmission and reflection coefficients, respectively. In Fig. 4, we plot the squares of these coefficients as functions of frequency observing that the identity $R^2 + T^2 = 1$ is only approximately met because of the small contributions coming from the QNMs frequency peaks in both the transmitted and reflected solu-

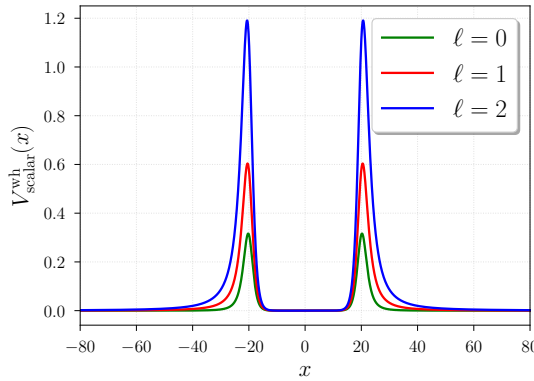


FIG. 5. Effective potential cavity for the wormhole, we observe the growth of the barriers with the quantum number ℓ .

tions. The shape of both the transmissivity and reflectivity curves is very similar to an hyperbolic tangent step function¹, intersecting at $R^2 = T^2 = 0.5$, as expected. Furthermore, it is crucial to notice from the last figure that it is only in a narrow band of frequencies where the amplitudes transmitted and reflected by the potential barrier are comparable. in the case of a wormhole, such a fact will be important in our analysis.

B. Scattering by a traversable wormhole

In this section, we study the dispersion of Gaussian wavepackets by a traversable wormhole, formed by the junction at $r_0 > r_g$ of two Schwarzschild black hole solutions with equal mass. There is a discontinuity in $G_{\alpha\beta}$ such that at $r = r_0 = 20.0r_g$, any contracting congruence of geodesics in one side of the throat starts to expand in order to reach the other side, violating the weak energy condition. The dynamics of the scattering problem is still given by the solutions of (1) following the same decomposition in spherical modes as in (5). Hence, the waveform of the equation of motion for the spherical modes is given by

$$[-\partial_t^2 + \partial_x^2 - V_{\text{scalar}}^{\text{wh}}(x)] \mathcal{U}_{\ell m}(x, t) = 0, \quad (10)$$

and the effective potential $V_{\text{scalar}}^{\text{wh}}(x)$ yields

$$V_{\text{scalar}}^{\text{wh}}(x) = \left(1 - \frac{r_g}{r(|x|)}\right) \left[\frac{\ell(\ell+1)}{r(|x|)^2} + \frac{r_g}{r(|x|)^3} \right]. \quad (11)$$

which is plotted in Fig. 5 and coincides with the shape of the potential calculated in [13]. Strictly speaking, we refer to $r(|x|)$ as the same inverse of the function mentioned

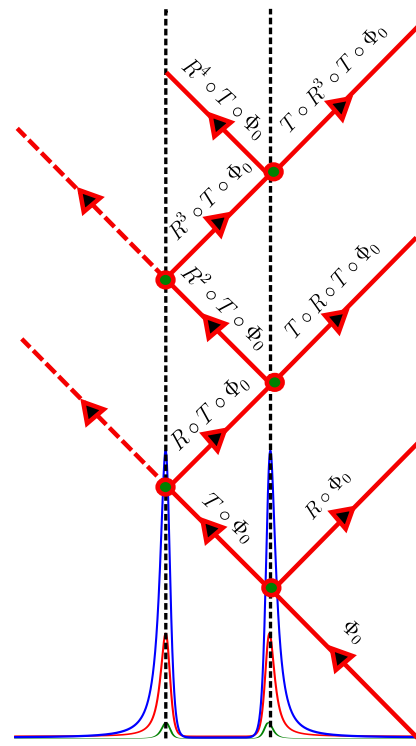


FIG. 6. Schematic reconstruction of the outgoing solution by a sequence of reflections and transmissions inside the potential cavity.

in (4) now evaluated at $|x| - r_0$. As we can see in Fig. 5, the new effective potential is merely a reflection of the potential barrier in Fig. 1 about the ordinate axis; thus, it is sensible to identify this system as a potential cavity built from two potential barriers with the reflection and transmission coefficients depicted in Fig. 4. Furthermore, let us assume that an arbitrary incident pulse Φ_0 propagates towards the cavity, it is, therefore, reasonable to approximate the spectrum of the asymptotic solution by a simple geometrical series of reflections and transmissions inside the cavity acting on the incident pulse, as shown in Fig. 6. Following this scheme, the asymptotic solution can be approximated by

$$\Phi^{\text{wh}}(\omega)|_{x \rightarrow +\infty} = \left[R + T \circ \sum_{i=0} \circ R^{2i+1} \circ T \right] \circ \Phi_0(\omega). \quad (12)$$

It is not difficult to see that, in the hypothetic case of a perfectly reflective wall replacing the left potential barrier in Figs. 5 and 6, the reconstructed pulse is instead given by

$$\Phi^{\text{f}}(\omega)|_{x \rightarrow +\infty} = \left[R + T \circ \sum_{i=0} \circ R^i \circ T \right] \circ \Phi_0(\omega), \quad (13)$$

corresponding to the case of a firewall. We will not cover the features of the firewall solution in what remains of this paper.

¹ This is not surprising after we consider the DeWitt approximation for the transmissivity [28], which is precisely given by a step function.

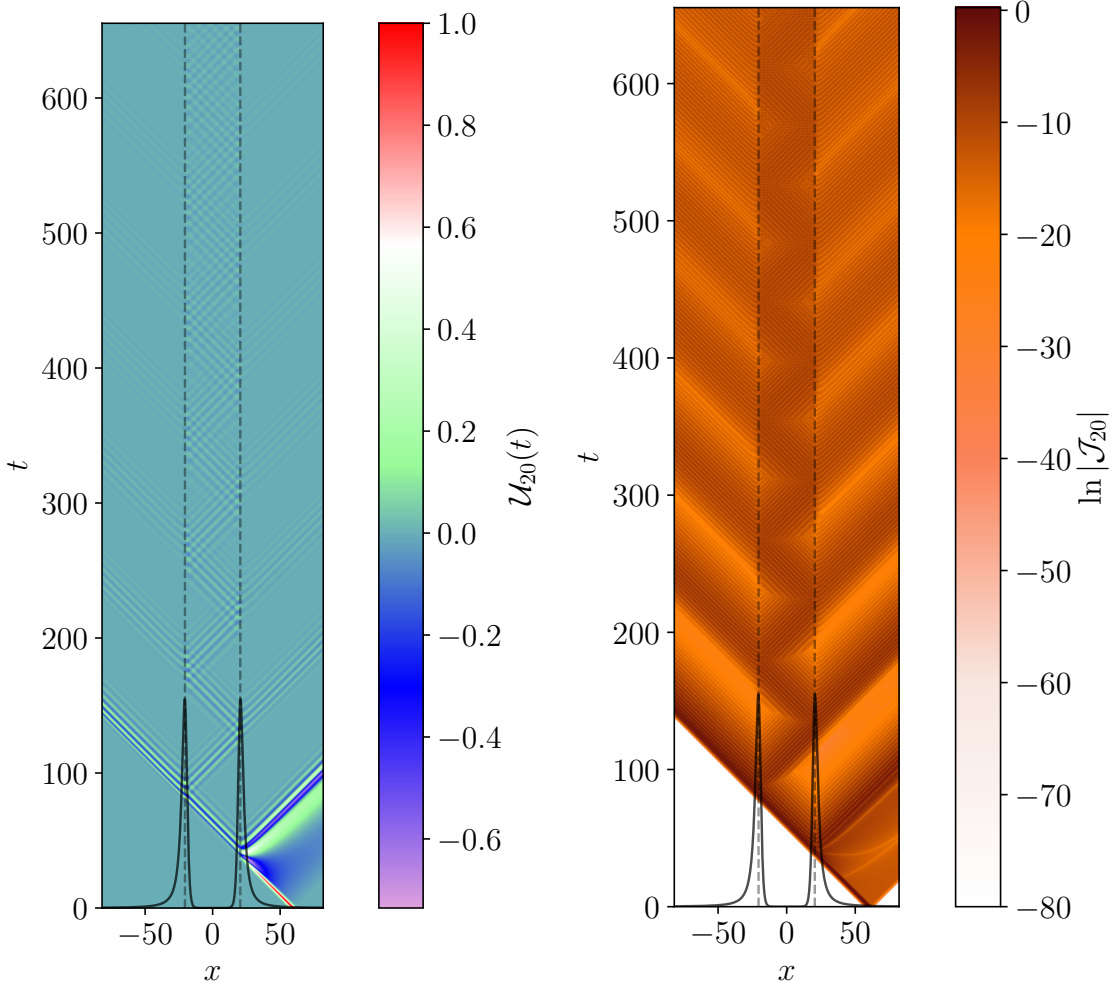


FIG. 7. Left panel: Evolution of the quadrupole mode \mathcal{U}_{20} for the effective potential in Fig. 5. We can notice the sequence of reflections and transmissions inside the cavity is very similar to the scheme depicted in Fig. 6. Right panel: Evolution of the radial flux $\mathcal{J}_{20} \equiv \mathcal{U}_{20,x}\mathcal{U}_{20,t}$, the only incident source comes from the collision of the pulse, which dissipates very slowly to the exterior every time the internal reflections hit the walls of the potential cavity. QNM are sourced by this process.

We now solve the scattering problem exactly for the quadrupole mode $\mathcal{U}_{20}(t, x)$. Using the same initial conditions as in (8) for $\sigma = 0.9185r_g$ as the width of the incident Gaussian pulse, we find the time-dependent solution of the quadrupole mode \mathcal{U}_{20} (left panel) and its radial flux $\mathcal{J}_{20} \equiv \mathcal{U}_{20,x}\mathcal{U}_{20,t}$ (right panel) in Fig. 7. It is interesting to notice in the evolution plot (on the left) that the signal forms an interference pattern at very late times, showing that this process might fill the cavity. In addition to this, even when the amplitude of the modes decreases after each collision against any of the potential walls, the spherical modes propagate for longer time throughout the spheres of maximal potential.

The scalar flux is shown in the right panel, we observe that the only source of scalar radiation comes from the first collision of the Gaussian wavepacket against the barrier in the right hand side (the ingoing flux is colored in black at the bottom of the contour plot). A sequence

of reflections occurs within the potential barriers, which decay in intensity with time as the cavity leaks energy to the exterior.

The amplitude of the outgoing signals depends on the width of the incident Gaussian wavepacket, this is visible in Fig. 8 where we plot the asymptotic solutions for two different ingoing wavepackets: one with $\sigma = 0.6495r_g$ in the left panel and a second one with $\sigma = 5.196r_g$ in the right. After subtracting the outgoing solution for a black hole, the presence of a train of wavelets, widely known as echoes, is very clear. The signal is not a straight line after the transient, as we can observe in the right panel of this figure. Therefore, subtracting the black hole outgoing pulse (i.e., the case in which there is only one potential wall) turns to be a convenient way to clean the signal from back reflections due to the “tails” of the potential barrier, especially since in this case the echoes are four orders of magnitude smaller than the transient. In both

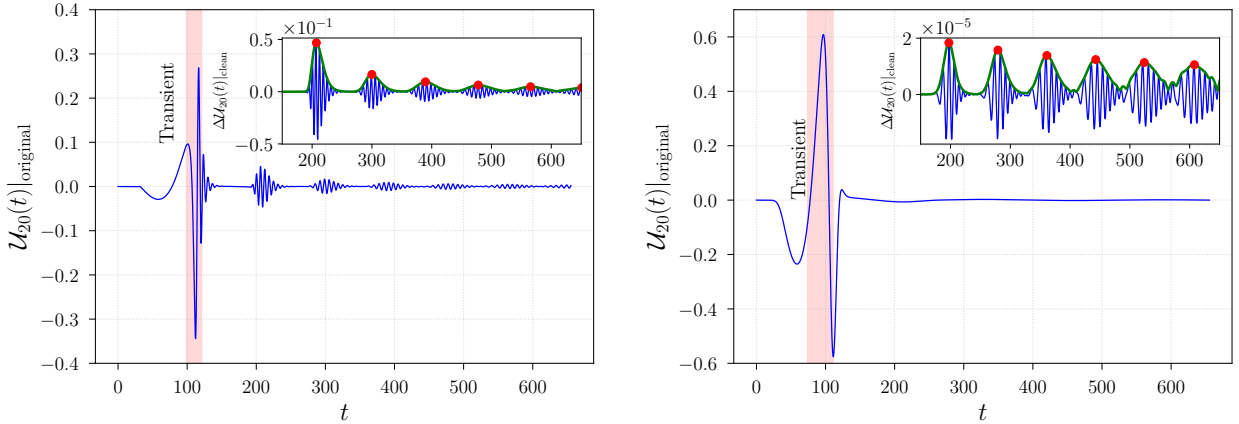


FIG. 8. Left panel: Asymptotic evolution of the quadrupole mode \mathcal{U}_{20} for $\sigma = 0.6495r_g$. Echoes are plotted in the upper corner of the plot, showing them along with their Hilbert envelope (the curves in green) and maximum amplitudes (in red). Right panel: Asymptotic evolution of the quadrupole mode \mathcal{U}_{20} for $\sigma = 5.196r_g$. In contrast with the left panel, echoes are four orders of magnitude smaller than the transient. The amplitude of the transient in the right figure has decreased with respect to the one in the left panel.

panels, we plot the variable $\Delta\mathcal{U}_{20}|_{\text{clean}} \equiv \mathcal{U}_{20}|_{\text{original}} - \mathcal{U}_{20}^{\text{bh}}$ in the right upper corner of the figures to represent the echoes and their net amplitude without backscattering effects.

As shown in subsection II A, the curves of reflectivity and transmissivity determine the frequencies going through the barriers of the potential cavity: most of the power of an incident pulse with large σ is in the low frequency domain, and therefore it will be reflected. Moreover, the cavity is transparent to high frequency signals, which are dominant in the pulses with small σ . In either of these extremal scenarios, QNMs cannot be sourced by internal reflections and thus, the amplitude of the echoes is not large in general.

Now we proceed to reconstruct the asymptotic spectrum by following the geometrical optics relation in (12) considering the reflectivity and transmissivity operators defined in (9). Then, the outcome should be compared with the spectral content of the asymptotic wave solutions of (10). We calculate the Fourier transforms of both the Gaussian incident pulse $\Phi_0(\omega) = \mathcal{F}[\exp((x - x_0)^2/2\sigma^2)]$ for $\sigma = 0.6495r_g$ and $x_0 = 60.0r_g$, and the asymptotic solution $\tilde{\mathcal{U}}_{20}^{\text{echo}} \equiv \mathcal{F}[\mathcal{U}_{20}(t, +\infty)]$, which includes the echoes.

After applying the reconstruction expression in (12) up to $i = 0$ (in red), and comparing the outcome with $\tilde{\mathcal{U}}_{20}^{\text{echo}}$, we show the reconstructed spectrum and $\tilde{\mathcal{U}}_{20}^{\text{echo}}$ (in blue) in Fig. 9. The low frequency oscillation peaks in the blue spectrum correspond to the finite size of the simulation box and should be ignored. Notice that the spectrum reconstructed employing the geometrical optics approximation gives the overall shape of the spectrum with de-

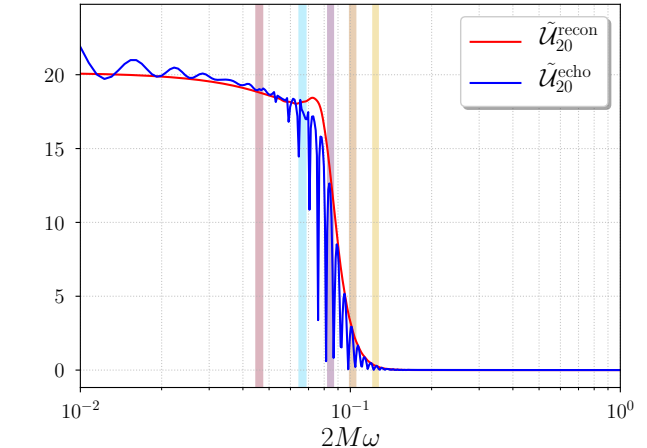


FIG. 9. Comparing the reconstruction of the spectrum by the geometrical optics approximation in (12) (in red) with the Fourier transform of the full asymptotic solution $\tilde{\mathcal{U}}_{20}^{\text{echo}}$ (in blue). The color stripes indicate a few of the first QNM frequency peaks corresponding to $\omega_3 = 0.251M^{-1}$ in golden rod, $\omega_4 = 0.207M^{-1}$ in peru, $\omega_5 = 0.169M^{-1}$ in plum, $\omega_6 = 0.133M^{-1}$ in light blue and $\omega_7 = 0.092M^{-1}$ in rosy brown, these are the real parts of the QNM frequencies for $n = 3, 4, 5, 6$ & 7 calculated in [18].

cent precision but not the QNM frequency peaks, these appear in the same frequency interval where the reflectivity and transmissivity curves intersect in Fig. 4. It is, therefore, reasonable to talk about a “sweet spot” in the frequency domain where the cavity maximizes the amplitude of the echoes. Intuitively, after observing the results in Fig. 8, it is possible to identify a similar “sweet spot” in the parameter space space for the widths of the incident Gaussian wavepackets. However, it is also necessary to

not only compare the amplitude of each individual echo with σ , but also the ratio between the amplitude of the echo with the amplitude of the transient for each value of the width.

III. SCATTERING OF TENSOR WAVEPACKETS

IV. CONCLUSIONS

-
- [1] B. P. Abbott *et al.* (LIGO Scientific, Virgo), *Phys. Rev. Lett.* **116**, 061102 (2016), arXiv:1602.03837 [gr-qc].
- [2] B. P. Abbott *et al.* (LIGO Scientific, Virgo), *Phys. Rev. Lett.* **116**, 241103 (2016), arXiv:1606.04855 [gr-qc].
- [3] A. V. Frolov, J. T. Gálvez Ghersi, and A. Zucca, *Phys. Rev.* **D95**, 104041 (2017), arXiv:1704.04114 [gr-qc].
- [4] V. Cardoso, E. Franzin, and P. Pani, *Phys. Rev. Lett.* **116**, 171101 (2016), [Erratum: *Phys. Rev. Lett.* 117,no.8,089902(2016)], arXiv:1602.07309 [gr-qc].
- [5] L. M. Krauss, S. Dodelson, and S. Meyer, *Science* **328**, 989 (2010), <http://science.sciencemag.org/content/328/5981/989.full.pdf>.
- [6] P. A. R. Ade *et al.* (BICEP2, Keck Array), Submitted to: *Phys. Rev. Lett.* (2018), arXiv:1810.05216 [astro-ph.CO].
- [7] T. Clifton, P. G. Ferreira, A. Padilla, and C. Skordis, *Phys. Rept.* **513**, 1 (2012), arXiv:1106.2476 [astro-ph.CO].
- [8] A. Taliotis, *JHEP* **05**, 034 (2013), arXiv:1212.0528 [hep-th].
- [9] A. Joyce, B. Jain, J. Khouri, and M. Trodden, *Phys. Rept.* **568**, 1 (2015), arXiv:1407.0059 [astro-ph.CO].
- [10] M. S. Morris, K. S. Thorne, and U. Yurtsever, *Phys. Rev. Lett.* **61**, 1446 (1988).
- [11] A. Almheiri, D. Marolf, J. Polchinski, and J. Sully, *JHEP* **02**, 062 (2013), arXiv:1207.3123 [hep-th].
- [12] P. O. Mazur and E. Mottola, (2001), arXiv:gr-qc/0109035 [gr-qc].
- [13] V. Cardoso, S. Hopper, C. F. B. Macedo, C. Palenzuela, and P. Pani, *Phys. Rev.* **D94**, 084031 (2016), arXiv:1608.08637 [gr-qc].
- [14] J. Abedi, H. Dykaar, and N. Afshordi, *Phys. Rev.* **D96**, 082004 (2017), arXiv:1612.00266 [gr-qc].
- [15] J. Abedi and N. Afshordi, (2018), arXiv:1803.10454 [gr-qc].
- [16] M. Visser, *Phys. Rev.* **D39**, 3182 (1989), arXiv:0809.0907 [gr-qc].
- [17] S. Chandrasekhar and S. L. Detweiler, *Proc. Roy. Soc. Lond.* **A344**, 441 (1975).
- [18] N. Andersson and S. Linnæus, *Phys. Rev. D* **46**, 4179 (1992).
- [19] T. Regge and J. A. Wheeler, *Phys. Rev.* **108**, 1063 (1957).
- [20] F. J. Zerilli, *Phys. Rev. D* **2**, 2141 (1970).
- [21] R. H. Price, *Phys. Rev. D* **5**, 2419 (1972).
- [22] R. H. Price, *Phys. Rev. D* **5**, 2439 (1972).
- [23] N. G. Sanchez, *Journal of Mathematical Physics* **17**, 688 (1976).
- [24] N. G. Sanchez, *Phys. Rev.* **D16**, 937 (1977).
- [25] N. G. Sanchez, *Phys. Rev.* **D18**, 1030 (1978).
- [26] N. G. Sanchez, *Phys. Rev.* **D18**, 1798 (1978).
- [27] L. Petrich, S. Shapiro, and I. Wasserman, *Astrop. J. Suppl. S* **58**, 297 (1985).
- [28] V. P. Frolov and I. D. Novikov, eds., *Black hole physics: Basic concepts and new developments*, Vol. 96 (1998).